POLITECNICO DI TORINO
Repository ISTITUZIONALE

Integrated seismic and electrical imaging with clustering for the hydro-mechanical screening of a high-altitude earthfill dam

Original
Integrated seismic and electrical imaging with clustering for the hydro-mechanical screening of a high-altitude earthfill dam / Strallo, V., Colombero, C., Godio, A.. - In: ENGINEERING GEOLOGY. - ISSN 1872-6917. - 375:(2026). [10.1016/j.enggeo.2026.109161]

Availability:
This version is available at: 11583/3016878 since: 2026-10-22T12:53:25Z

Publisher:
Elsevier

Published
DOI:10.1016/j.enggeo.2026.109161

Terms of use:

This article is made available under terms and conditions as specified in the corresponding bibliographic description in the repository

Publisher copyright

(Article begins on next page)

15 November 2026

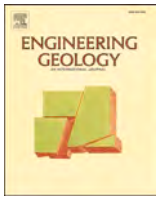
Engineering Geology 375 (2026) 109161



Contents lists available at ScienceDirect

Engineering Geology

journal homepage: www.elsevier.com/locate/enggeo



Integrated seismic and electrical imaging with clustering for the hydro-mechanical screening of a high-altitude earthfill dam☆

Valeria Strallo *, Chiara Colombero, Alberto Godio

Politecnico di Torino, Department of Environmental, Land and Infrastructure Engineering (DIATI), Turin, Italy

ARTICLE INFO

Keywords:
Geophysical characterization
Alpine infrastructures
ERT
Active seismic

ABSTRACT

Earthen dams located in high mountain environments are exposed to intense environmental stresses due to strong freeze-thaw cycles that can affect material integrity. Climate change can further amplify these stresses through the increasing frequency of extreme events and natural hazards. At the same time, their remote locations and hostile environmental conditions may be challenging for monitoring instrumentation. For this reason, a preliminary and comprehensive characterization of these infrastructures is fundamental to define the best monitoring strategies. In this study, we conducted an integrated geophysical characterization of an Alpine artificial reservoir (Fourcare dam, Aosta Valley), to monitor the water infiltration processes within the dam. We combined Electrical Resistivity Tomography (ERT) and active seismic surveys, including both seismic refraction tomography and surface wave analyses, to investigate the hydrological and mechanical properties of the embankment. To integrate the parameters resulting from the two geophysical methods and identify potentially critical subsurface layers, we applied clustering of the obtained electrical resistivity data and seismic parameters (i.e. shear wave velocity and surface wave autospectral density). The joint use of ERT and seismic methods, together with the cluster analysis, provided a consistent and physically coherent framework for the identification of anomalies potentially linked to hydraulic infiltrations, supporting the non-invasive screening of this remote alpine infrastructure.

1. Introduction

Earthfill dams and embankments are the most common structures worldwide due to their low construction costs. These infrastructures play a critical role in water resource storage and management, agriculture, and natural hazard mitigation (Al-Janabi et al., 2020; Baxter, 1977; FAO, 2010; Omofunmi et al., 2017; Yener Ozkan, 1998).

While the structural stability and safety of large dams are subject to detailed monitoring and national regulation because of their recognized hazard potential, small dams often receive less attention (Pinto and Fais, 2023; Kasana et al., 2015). However, due to their widespread presence and older, less stringent construction standards, they are particularly vulnerable to aging, degradation and collapse, which can damage the environment, nearby communities and infrastructures (Bocchiola and Rosso, 2014; Bozzoni et al., 2023; Ciancimino et al., 2023; Pisaniello et al., 2015).

Dams located in Alpine and high-altitude environments (higher than 2000 m a.s.l.) are exposed to exceptional environmental and climatic stresses, including intense freeze-thaw cycles, extreme events and consequent natural hazards (Strozzi et al., 2018; Wu et al., 2023). Climate change can further compromise the integrity of earth-filled dams in several ways. Intense rainfall promotes surface erosion and structural damage, while summer droughts can cause drying and cracking of dam materials, creating preferential pathways for water infiltration and accelerating structural deterioration (Li et al., 2019; Liu et al., 2024; Koyama et al., 2022). Additionally, natural hazards, such as landslides linked to permafrost degradation, can pose further risks related to the stability of these infrastructures (Duvillard et al., 2019; Gruber et al., 2004; IPCC, 2019). Any pre-existing structural defect or weakness can thus be rapidly enhanced under these conditions, increasing the risk of sudden failure (Ayadat, 2019; Ziccarelli and Rosone, 2021).

Assessing the structural integrity of these infrastructures is further complicated by their remote and hard-to-access location, which limits the feasibility of continuous monitoring and periodic site inspections. Furthermore, available geological and geotechnical information for

☆ This article is part of a Special issue entitled: 'Geophysics to aid Geomodeling' published in Engineering Geology.

* Corresponding author.
E-mail address: valeria.strallo@polito.it (V. Strallo).

https://doi.org/10.1016/j.enggeo.2026.109161
Received 2 March 2026; Received in revised form 16 October 2026; Accepted 19 October 2026
Available online 20 October 2026
0013-7952/© 2026 The Authors. Published by Elsevier B.V. This is an open access article under the CC BY license (http://creativecommons.org/licenses/by/4.0/).

small alpine dams is typically sparse and confined to point measurements, providing an incomplete picture of the spatial variability in embankment materials and internal conditions. Monitoring instrumentation, where present, requires periodic manual acquisition, further limiting the temporal continuity of the available data.

In this context, geophysical methods represent a particularly valuable tool for non-invasive, spatially continuous characterization of the subsurface, compensating for the absence of dense geotechnical data. Among the available techniques, Electrical Resistivity Tomography (ERT) and active seismic surveys have been widely applied to embankment characterization, proving effective in detecting heterogeneities, seepage pathways and areas of reduced mechanical properties (e.g., Adamo et al., 2020; Camarero and Moreira, 2017; Cardarelli et al., 2014; Kayode et al., 2018; Loperte et al., 2016; Michalis et al., 2016; Ólafsdóttir et al., 2019; Panthulu et al., 2001; Perri et al., 2014). Due to its sensitivity to water content variations, ERT is effective in detecting the presence of saturated zones or potential leakages, while seismic methods provide estimates of material stiffness and mechanical integrity. The integration of both methods improves the interpretation and spatial delineation of potential internal structural weaknesses.

When geotechnical reference data are scarce, however, the interpretation of individual geophysical parameters alone may be ambiguous. Integrating multiple physical properties within a multivariate framework allows for a more reliable discrimination of subsurface units, reducing interpretative uncertainty.

Clustering approaches, such as Gaussian Mixture Models (GMM), provide an effective way to identify spatially coherent domains from the joint distribution of complementary geophysical parameters, helping to characterize subtle anomalies potentially associated with internal erosion, moisture distribution, and mechanical degradation (e.g., De Donno et al., 2024; Linde and Doetsch, 2016).

Despite the growing literature on geophysical investigation of embankments, the integrated application of ERT, seismic methods and multivariate clustering to small, high-altitude structures, where both environmental stresses and data scarcity are most critical, remains limited.

We focus on a geophysical investigation of the Fourcare dam (northwestern Italian Alps), a small alpine embankment for which only

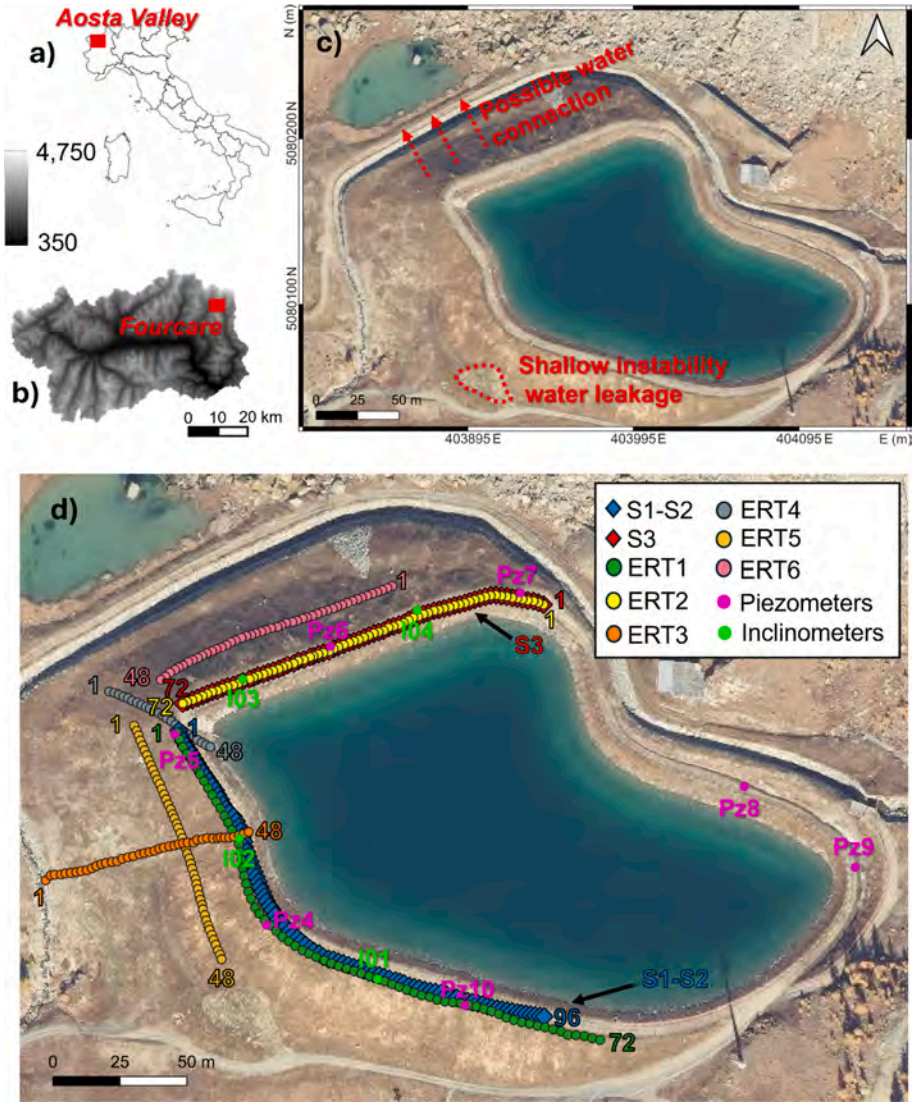


Fig. 1. (a) Geographical location of the Fourcare dam (Aosta Valley, northwestern Italian Alps). (b) DTM of the Aosta Valley region (https://mappe.regione.vda.it/pub/geonavitg/geodownload.asp?carta=DTM99, last access on September 3, 2024). (c) Fourcare dam test site showing the possible areas of water leakage or seepage highlighted in red. (d) location of the ERT and seismic lines, together with the piezometers (magenta dots) and inclinometers (green dots). Numbers on seismic lines indicate the first and last geophones of each line, while on ERT profiles they indicate the first and last electrodes. (For interpretation of the references to colour in this figure legend, the reader is referred to the web version of this article.)

limited geotechnical point data are available. We combined ERT and active seismic surveys (P-wave refraction and surface wave analysis), and integrated the retrieved parameters (electrical resistivity, shear-wave velocity, and surface wave autospectral density) within a GMM clustering framework to obtain a spatially coherent picture of the embankment's internal conditions. Available geotechnical information of the site consists primarily of pre-construction borehole logs and design documentation. These data characterize the ante-operam stratigraphy and define the intended geometry of the embankment, but do not constrain the current internal state of the dam, its actual spatial variability, or the distribution of moisture and mechanical properties after years of operation under alpine climatic stresses.

The primary aim of this work is to characterize the internal structure of the embankment, identifying spatially coherent zones of potential weakness, moisture anomalies, and seepage, while assessing the applicability of integrated geophysical approaches for the non-invasive screening of remote alpine infrastructure where conventional monitoring data remain sparse and discontinuous.

2. Test site

The selected site for this study is the Fourcare dam. Located within the northwestern sector of the Aosta Valley (northwestern Italy, Fig. 1a), this artificial earthfill dam is close to the Bettaforca chairlift station, at an elevation of approximately 2325 m on the watershed between the Ayas and Gressoney Valleys (Fig. 1b). Its construction was commissioned by Monterosa S.p.A. to support the snowmaking system between the localities of Fourcare-Damon and Frachey. The dam serves as a water reservoir for the production of artificial snow used in the surrounding ski facilities (Fig. 1c), supplied by a diversion from the Fourcare stream.

The site is characterized by heterogeneous glacial deposits in a sandy-silty matrix, overlying a bedrock mainly composed of serpentinites. The bedrock is encountered at depths higher than 15 m, although its depth may vary locally. The upper part of the bedrock is more fractured, becoming progressively more compact with increasing depth. The reservoir was constructed by excavating a natural flat area formed along the mountain slope. Excavation mainly affected the northern, western, and southern sides, where the removed material was reused to construct the embankments enclosing the basin. On the eastern side, adjacent to the descending mountain slope, excavation was limited and mainly involved bedrock, with no significant lateral cut slopes.

An impermeable geomembrane of 2.5-mm thickness was installed at the bottom of the basin to ensure water retention, covering the entire internal surface of the reservoir from the base up to the crest of the embankments. The lining was anchored within a trench excavated along the crest road and subsequently backfilled with finer materials to hydraulically isolate the reservoir from the embankment body and the surrounding hydrogeological system. The resulting stratigraphy, as inferred from pre-construction borehole logs and design documentation, is reported in Fig. 2. It consists of a superficial fine-grained layer, underlain by reworked and mechanically compacted coarser materials, followed by undisturbed glacial deposits, and finally by the serpentinite bedrock. A topsoil layer with vegetation cover was subsequently placed on the embankment surface to promote integration with the surrounding landscape. The height of the earthfill dam on the northern and western sides is approximately 15 m. The water basin has an extension of approximately 21,000 m^2 and a maximum depth of 12.5 m.

Sporadic water seepages have been observed on the southern face of the reservoir embankment (Fig. 1c). Additionally, a small lake is located immediately northwest of the basin (Fig. 1c), although its potential hydraulic connection with the artificial reservoir remains unknown.

The site is equipped with seven piezometers and four inclinometers along the crest of the dam, all located at the same elevation (Fig. 1d). These monitoring points have been frequently surveyed since their construction, and the measurements are summarized in Fig. 3 and Fig. 4.

The piezometers are open pipe installations reaching a depth of 20 m and are not hydraulically connected to the reservoir water level, providing information on groundwater conditions within the dam body and surrounding shallow foundation materials. Piezometric data (Fig. 3a) reveal a heterogeneous water table regime in the basin perimeter, with a clear difference in behaviour between the upstream (Pz7–8-9) and downstream (Pz4–5–6-10) sectors. Pz7–8-9 show a relatively stable and persistently high-water level, with limited sensitivity to seasonal variations. This behaviour reflects sustained groundwater recharge from the upslope catchment area, which is characterized by fractured rock masses, small ponds, and surface runoff channels that enhance infiltration processes. The combination of topographic convergence and continuous recharge results in a more stable saturated condition in the upstream sector. In contrast, Pz4–5–6-10 show a more dynamic response to meteorological forcings, with rapid increases in water table depth following precipitation events. During the spring snowmelt period, these piezometers exhibit an initial rise in groundwater levels, associated with transient infiltration of meltwater into the shallow subsurface. This is followed by a gradual decrease in water table depth despite continuing temperature increase, indicating that drainage processes progressively dominate over recharge in a steep slope setting. The average reservoir water level (Fig. 3a) shows a dependence on precipitation events but is primarily controlled by regulated inflows from the partial diversion of the Fourcare stream and by water extraction for snowmaking purposes.

The inclinometer tubes cross the embankment section and extend into the underlying undisturbed ground up to 20-m depth. Inclinometer

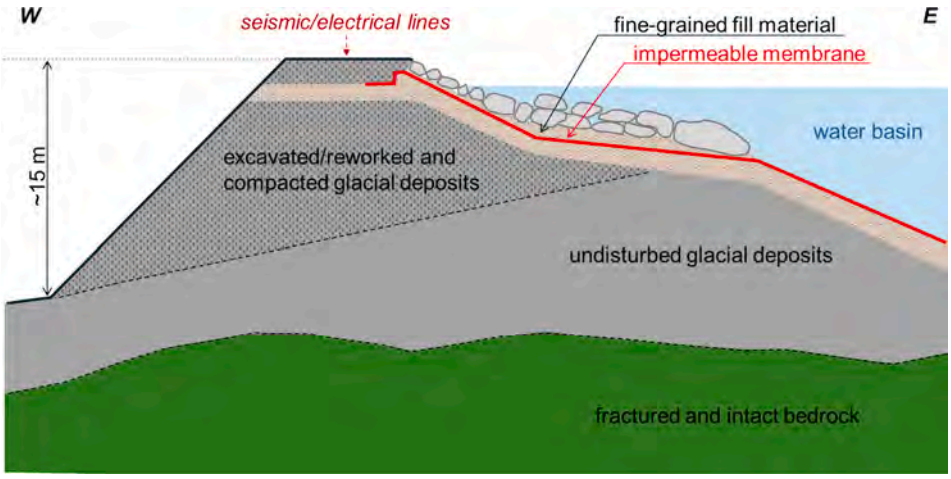


Fig. 2. Representative cross-section of the embankment and stratigraphy of the western side of the reservoir.

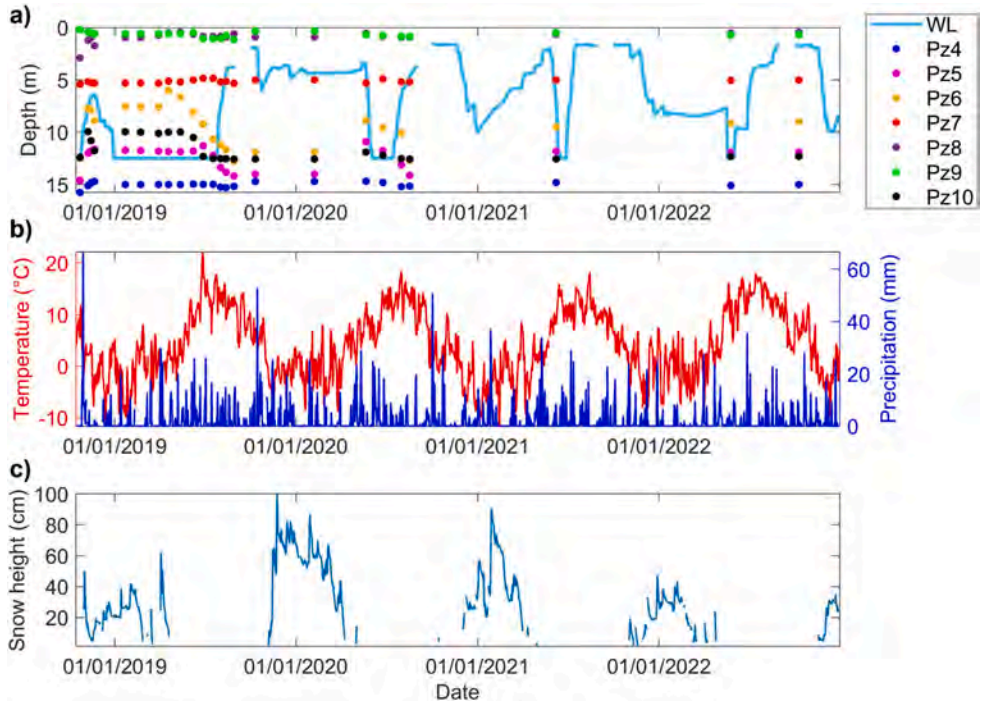


Fig. 3. (a) Water table depth below ground surface recorded in piezometers (dots) and water level within the reservoir (solid line) during the monitoring period from 2018 to 2023, with measurements conducted at approximately 6-week intervals. (b) Temperature (red) and precipitation (blue) data acquired at the nearby Ayas - Alpe Aventine weather station. (c) Snow height at ground level acquired at the same station (https://presidi2.regione.vda.it/, last access on April 15, 2026). (For interpretation of the references to colour in this figure legend, the reader is referred to the web version of this article.)

I02 (Fig. 4b) recorded a localized displacement within the 5–8 m depth interval in both directions, reaching maximum cumulative values of approximately 3.7 mm (*E*-W direction) and 1.8 mm (N-S direction) at 6.5–7 m depth between February 2019 and June 2023 (about 0.8 and 0.4 mm/yr, respectively). This localized deformation occurs in the same sector where sporadic water seepage has been observed. Inclinometer I03 (Fig. 4c) recorded a localized displacement within the 6–12 m depth interval in the E-W direction, reaching a maximum cumulative value of approximately 9.3 mm at 9 m depth between March 2019 and June 2023 (about 2.2 mm/yr on average). The recorded displacements show a progressive trend over the monitoring period, suggesting cumulative time-dependent deformation rather than seasonal reversible movements. The depth at which these deformations occur suggests that displacements are concentrated at the interface between the embankment fill and the undisturbed glacial deposits, where the contrast in mechanical properties between the compacted fill and the more competent foundation material is most pronounced.

The observed seepage phenomena and the localized deformations detected by the inclinometers raise concern about the presence of preferential flow paths and potential zones of mechanical weakness within the embankment. However, the available geotechnical data are primarily ante-operam and confined to point measurements, while monitoring instrumentation provides only spatially sparse observations along the dam crest. Neither dataset allows a spatially continuous characterization of these processes or an unambiguous identification of their origin, nor do they constrain the current internal state of the embankment after years of operation under alpine climatic stresses. For this reason, a geophysical characterization campaign was conducted to investigate the internal structure of the dam and identify potential leakage pathways and zones of mechanical weakness that may affect its stability.

Six Electrical Resistivity Tomography lines (ERT1 to ERT6, in Fig. 1d) were acquired on the crest and the slopes of the embankment. Additionally, three active seismic lines (S1-S2 and S3, Fig. 1d) were acquired along the dam crest. S1 and S2 were acquired along a common profile, with line S2 partially overlapping S1 starting from the position of the 25th geophone. For processing and interpretation purposes, the two datasets were merged and treated as a single extended spread, hereafter referred to as S1–S2. Both ERT and seismic acquisitions were performed on the same day under consistent environmental conditions, in order to ensure comparability between datasets and to minimize the influence of temporal variability (e.g., moisture and temperature changes) on the measured parameters. The geophysical survey lines were designed to investigate the embankment body and do not intersect the geomembrane lining, which is confined to the internal surface of the reservoir.

3. Methods

3.1. Electrical lines

Six ERT lines were acquired in different locations surrounding the water basin using a variable number of electrodes connected to a Syscal Pro (IRIS Instrument) resistivity meter. ERT1, located on top of the south-west crest of the dam, consisted of 72 electrodes at 3-m spacing, covering a total length of 213 m. ERT2 was acquired on the north side of the embankment with 72 electrodes at 2-m spacing, for a total length of 142 m. ERT3 and ERT4 were acquired along the maximum slope of the western embankment, with 48 and 24 electrodes respectively, at 2-m spacing (total length of 94 m and 46 m), while ERT5 and ERT6 were conducted parallel to the embankment slope, on the western and northern slopes respectively, employing 48 electrodes at 2-m spacing (total length 94 m). To optimize the sensitivity to spatial variations in resistivity and the depth of investigation, all ERT profiles were acquired using two sequences of Wenner-Schlumberger and dipole-dipole array configurations. The main acquisition parameters and number of electrical measurements are summarized in Table 1. As a pre-processing of the data, outlier measurements, identified by a standard deviation of apparent resistivity exceeding 4%, were filtered out to improve the reliability of the inversion. Inversion was then performed using the

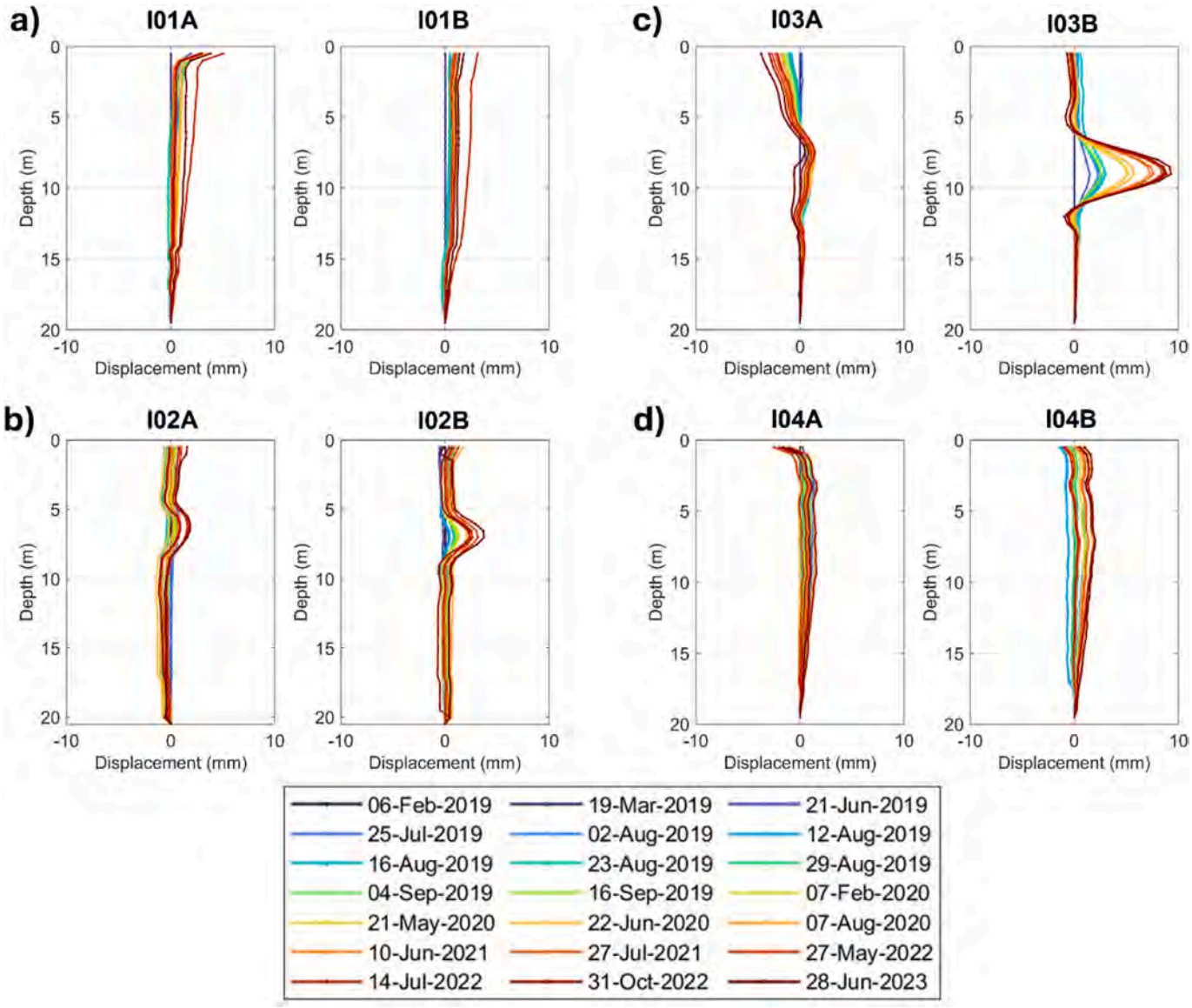


Fig. 4. (a to d) Displacement data from the inclinometers collected between 2019 and 2023 (A and B refer to the orthogonal measurements aligned with the N-S and E-W directions, respectively): (a) I01, (b) I02, (c) I03, (d) I04.

Table 1
Summary of ERT lines parameters and number of electrical measurements.

ERT Line	N° of electrodes	Spacing (m)	Total length (m)	N° of measurements (WS)	N° of measurements (DD)
ERT1	72	3	213	1286	1285
ERT2	72	2	142	1287	1286
ERT3	48	2	94	587	618
ERT4	24	2	46	191	207
ERT5	48	2	94	437	829
ERT6	48	2	94	871	900

open-source software ResIPy (Blanchy et al., 2020). Wenner-Schlumberger and dipole-dipole profiles were inverted separately and jointly to enhance the imaging capabilities along each line.

3.2. Seismic lines

The seismic data were collected along two main lines, S1-S2 and S3. S1-S2, acquired along the same profile of ERT1, consisted of 96 geophones in total, with a spacing of approximately 2 m, reaching a total length of 190 m. S3 was positioned along the same profile of ERT2, and consisted of 72 geophones with a 2-m spacing, with a total length of 142 m. An 8 kg sledgehammer striking a metal plate was used as the active seismic source. For both lines, starting from the first geophone, the source was positioned every 4 geophones, and each shot was repeated 5 times at each location to allow for trace stacking. All survey lines employed 4.5 Hz vertical geophones connected to a Geode acquisition system (Geometrics). All traces were acquired with a sample rate of 6.25E-05 s for a total length of 0.8 s, to allow for both first arrival time picking and surface wave analysis, and a pre-trigger window of 0.1 s.

3.2.1. Seismic refraction tomography

To obtain a P-wave velocity (V_P) model of the embankment and underlying material, we used a standard seismic refraction tomography approach. First-arrival times were picked manually on the stacked traces acquired at each source position, and a relative uncertainty of 3% was assigned to the picked traveltimes. The traveltimes were then inverted using pyGIMLi (Rücker et al., 2017) over 2D triangular meshes (maximum cell area 5 m^2, with five secondary nodes per cell edge for the

forward calculation), starting from a vertical gradient velocity model (500–5000 m/s). A smoothness-constrained inversion was applied with a regularization parameter λ=20. Iterations were stopped when the relative decrease of the data misfit fell below 2% (maximum 20 iterations).

3.2.2. Surface wave analysis

To obtain a shear-wave velocity (V_S) model we carried out surface wave analysis on the same traces adopted for first arrival time picking. In detail, we applied a moving window of 12 receivers to both S1-S2 and S3 lines. For each window, we computed the frequency-phase velocity spectrum through the phase shift method (Park et al., 1998). The spectra of the recordings of the same window obtained from different source locations were stacked to increase the signal-to-noise ratio (Neducza, 2007). The dispersion curves related to the fundamental mode of Rayleigh waves were then picked as the maxima of the stacked spectra. Each dispersion curve was assigned to the centre of the window. The dispersion curves along each line were inverted with a laterally constrained inversion approach based on Auken and Christiansen (2004), which was customized for surface wave inversion by Boiero (2009) and modified by Khosro Anjom et al. (2024). At each iteration the V_S and thicknesses of an initial model are updated, while the Poisson's ratio and density are fixed a priori. All the DCs are inverted simultaneously for a set of 1D models tied by lateral constraints on thicknesses and velocities between neighbouring models, and by vertical constraints between adjacent layers. The initial model consisted of six layers over a half-space, with thicknesses of 3 m for the four uppermost layers and 5 m for the two deeper ones, and V_S increasing from 300 m/s in the shallowest layer to 1500 m/s in the half-space. Poisson's ratio was fixed at 0.25, and density was fixed at values increasing with depth from 1800 to 2700 kg/m^3. An uncertainty of 50 m/s was assigned to the picked phase velocities. The inversion was run for a fixed number of 39 iterations, after which the change in global misfit between consecutive iterations was below 0.5% for both lines.

In addition, we also computed a fast surface wave attribute sensitive to the presence of sharp lateral variations on the raw seismic data (Colombero et al., 2019). This attribute, known as autospectrum, is the autospectral density $G_i(f)$ of each seismic trace $y_i(t)$ along the line, computed as the sum of the squares of the real and imaginary components of its discrete Fourier transform $Y_i(f)$, following

$$G_i(f) = \{Re[Y(f)]\}^2 + \{Im[Y(f)]\}^2 \quad (1)$$

The computation is repeated for each available shot position along the line and the autospectral values of each trace are multiplied for the distance from the source and then normalized to their maximum value. After this correction, all the autospectra related to the same receiver position are stacked to improve the coverage along the line. High autospectral values are expected in correspondence of weak and low-velocity materials. As a consequence, the method can quickly and effectively reveal some heterogeneities and weaknesses inside the earth dam. Since the attribute is frequency dependent, it also gives an estimation of the depth of the anomaly. In particular, the dispersion curves extracted along the lines can help in the conversion of the frequencies into wavelengths. A rough estimate of the depth of the anomaly can then be obtained by dividing the wavelengths by 3, that roughly corresponds to the depth of maximum displacement of the surface waves (Colombero et al., 2019).

3.3. Clustering

Four parameters were retrieved from the geophysical investigations acquired on the crown of the dam (S1-S2 and S3), i.e. electrical resistivity, P-wave velocity, S-wave velocity, and autospectral density. Between the four parameters, V_P showed a relatively smooth spatial distribution with limited variability compared to electrical resistivity, V_S and autospectral density. For these reasons, it was excluded from the clustering to improve cluster separability and discrimination of different materials. Electrical resistivity, V_S and autospectral density showed instead higher spatial variability and contrast. They were resampled to a common 2D grid to enable clustering. The analysis was restricted to the central portion of the sections, where all parameters overlap and data coverage is highest, while peripheral areas were excluded to avoid potential edge effects and reduced data reliability. To reduce the strong skewness in magnitude and improve cluster separability, the three selected parameters were transformed in log10 scale (De Donno et al., 2024). The optimal number of clusters (k) was estimated using the elbow method applied to k-means clustering. For k = 1 to 10, the within-cluster sum of squares (WCSS) was computed as the sum of squared distances between each data point and its assigned centroid. The WCSS curve was analyzed to identify the inflection point beyond which adding clusters no longer produced a significant reduction in intra-cluster variance. This preliminary analysis suggested a partition into three clusters.

A GMM with three components (k = 3) was consequently fitted to the log-transformed data. Each Gaussian component represents a potential cluster, parameterized by a mean vector and full covariance matrix. Each observation was assigned to the component with the maximum a posteriori (MAP) probability, and the posterior probability P(x) was used as a quantitative measure of classification confidence (McLachlan and Peel, 2000). Cluster quality was quantitatively assessed using the silhouette coefficient calculated from the MAP assignments. Because the silhouette coefficient is based on distances between observations, it was computed in the z-score-standardized log-transformed parameter space, to ensure a comparable contribution from electrical resistivity, V_S, and autospectral density. Standardization was applied only for the calculation of the silhouette coefficient and did not alter the GMM fitting procedure. The silhouette coefficient ranges from −1 to 1, with positive values indicating that observations are, on average, closer to their assigned cluster than to neighbouring clusters. Clustering robustness and classification confidence were additionally summarized using the mean and median maximum posterior probability, the percentages of observations with $P_{max} > 0.8$ and $P_{max} > 0.9$. However, these indicators assess the internal consistency and separation of the clusters within the geophysical parameter space, but do not represent validation against independent hydrogeological or geotechnical ground truth.

Cluster indices were then replotted back into their spatial position to assess the presence of different layer or zones characterized by different materials. The transparency of each point was scaled according to P(x), pixels with $P \leq 0.5$ were rendered fully transparent, while those with $P = 1$ appeared fully opaque. This approach highlights areas of robust classification while suppressing uncertain zones, allowing a direct visualization of model confidence.

To validate the exclusion of V_P from the clustering, the procedure was repeated including it as an additional parameter. Preliminary results confirmed that its inclusion does not improve cluster separability and may reduce the sensitivity of the procedure, supporting the decision to exclude it from the final analysis.

4. Results

The results of the electrical resistivity tomographies acquired on the earth dam are summarized in Figs. 5 to 7. In general, all the lines show a shallow discontinuous layer (0–5 m depth) characterized by high resistivity values (>800 Ωm). At greater depths, resistivity decreases, locally reaching values close to 100 Ωm within portions of the dam body and near its base. At depths greater than approximately 15–20 m from the crest, resistivity values increase again, exceeding 3000 Ωm, consistent with the presence of more compacted materials at depth.

For the lines acquired along the dam crest, the conductive zone appears deeper along ERT1, between 75 and 100 m along the profile (Fig. 5b), while ERT2 (Fig. 5d) shows more uniform resistivity

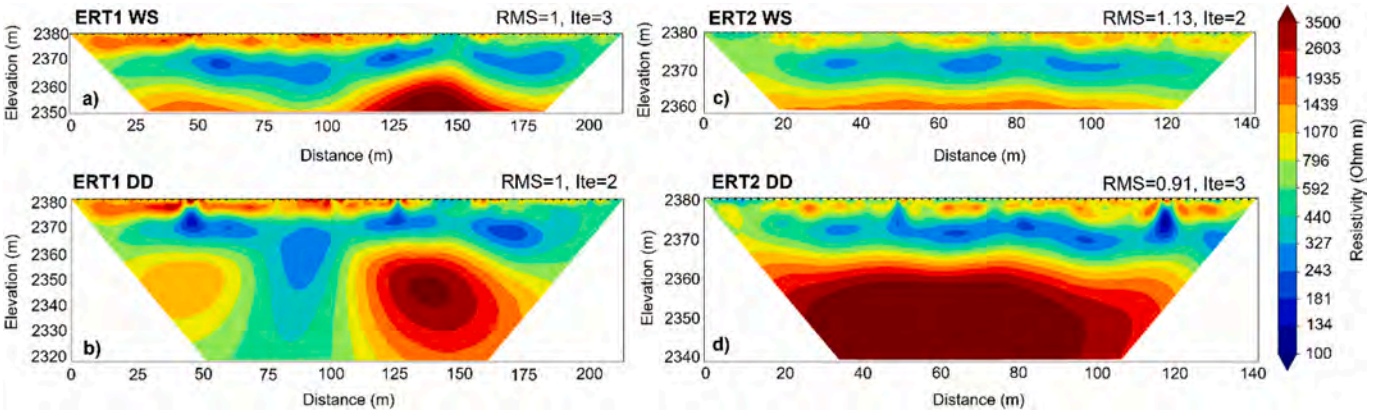


Fig. 5. Inversion results of ERT1 and ERT2 obtained with Wenner–Schlumberger (WS) and dipole–dipole (DD) arrays. Panels (a)–(b) refer to ERT1 and panels (c)–(d) to ERT2. The iteration number and the corresponding RMS misfit are indicated at the top of each panel.

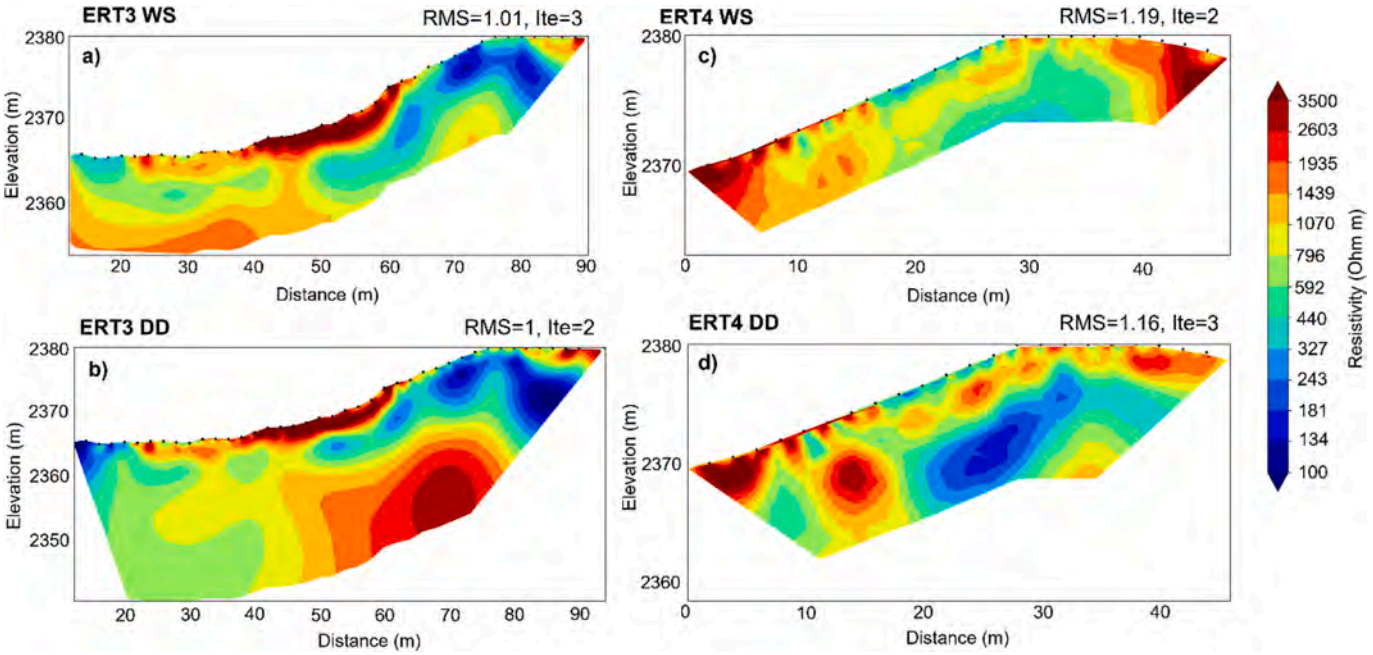


Fig. 6. Inversion results of ERT3 and ERT4 obtained with Wenner–Schlumberger (WS) and dipole–dipole (DD) arrays. Panels (a)–(b) refer to ERT3 and panels (c)–(d) to ERT4. The iteration number and the corresponding RMS misfit are indicated at the top of each panel.

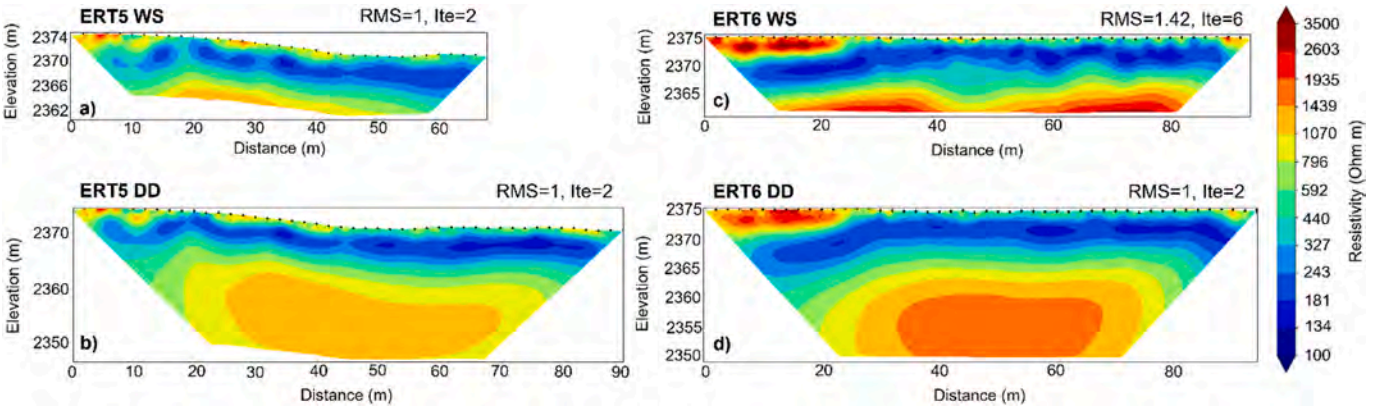


Fig. 7. Inversion results of ERT5 and ERT6 obtained with Wenner–Schlumberger (WS) and dipole–dipole (DD) arrays. Panels (a)–(b) refer to ERT5 and panels (c)–(d) to ERT6. The iteration number and the corresponding RMS misfit are indicated at the top of each panel. The profile for Wenner–Schlumberger configuration of ERT 5 (panel a) was cut at 70 m due to an issue occurred during the acquisition phase at the end of the line.

distribution without pronounced lateral anomalies. For the downslope lines a localized low-resistivity anomaly is observed at 10-m depth in the upper part of ERT3 (Fig. 6b) and in the central portion of ERT4 (Fig. 6d). ERT5 and ERT6 show a resistivity distribution consistent with the general pattern described above, without pronounced lateral anomalies (Fig. 7). The 3D visualization of the ERT results (Fig. 8) shows good agreement at line intersections, enabling a coherent reconstruction of the subsurface.

Seismic results along lines S1–S2 and S3 are shown in Figs. 9 and 10, together with the corresponding resistivity sections and derived elastic parameters. P-wave velocity (V_P) generally increases with depth in both sections. In contrast, S-wave velocity (V_S) models show velocity inversions within the upper 15 m.

A layer characterized by low V_S values (approximately 500 m/s), centred around 10 m depth, is consistently observed. This feature is also associated with high Poisson's ratio values (0.4–0.5) and elevated autospectral values. The same depth interval corresponds to relatively low resistivity values in the electrical sections.

Along line S1–S2, inclinometer I02 shows a localized displacement within the 5–8 m depth interval. This interval corresponds to a marked V_S inversion and elevated autospectral values. In contrast, inclinometer I01 (Fig. 4a), located in a different sector of the embankment, does not show localized displacement and corresponds to a thinner zone of low V_S and autospectral values.

Along line S3, inclinometer I03 recorded displacements within the 6–12 m depth interval. Although located outside the V_S model extent, this depth interval corresponds to relatively high autospectral values.

The clustering results integrating resistivity, V_S, and autospectral data are presented in Fig. 11. Cluster 1 is characterized by higher resistivity and V_S values and lower autospectral amplitudes. Clusters 2 and 3 show similar V_S values, but cluster 2 is distinguished by lower resistivity and higher autospectral values.

The median values of each parameter, together with the proportion of observations assigned to each cluster, are reported in Table 2.

The three-component solution yielded a mean silhouette coefficient of 0.275. Approximately 10.3% of the observations showed negative silhouette values. The mean and median maximum posterior probabilities were 0.904 and 0.964, respectively, with 81.8% of the observations characterized by $P_{max} > 0.8$ and 70.7% by $P_{max} > 0.9$. These results indicate generally high classification confidence but only partial geometric separation among the clusters, consistent with the presence of gradual transitions and overlapping hydro-mechanical properties within the investigated materials.

5. Discussion

The combined analysis of electrical resistivity and seismic data provides a consistent picture of the internal structure of the embankment with its expected stratigraphy. The shallow high-resistivity layers are interpreted as unsaturated surface zones, while the underlying conductive regions are indicative of increased moisture content. These results are consistent with previous studies applying integrated ERT and seismic methods to embankment characterization, while extending their application through a clustering-based integration in a high-altitude alpine setting. Cardarelli et al. (2014) combined ERT, P- and SH-wave tomography, and surface-wave analysis to reconstruct the geometry and low-strain elastic properties of an earth-filled dam, showing that electrical and seismic parameters provide complementary constraints on moisture conditions and material stiffness. Loperte et al. (2016) used an integrated geophysical approach to characterize water infiltration within a rock-fill dam, whereas Himi et al. (2018) combined ERT, seismic refraction tomography, and electromagnetic measurements to identify preferential seepage and monitor remediation through mortar injection. Vagnon et al. (2022) further demonstrated the potential of combined electric and seismic measurements for the hydraulic characterization of an earth dam when suitable geotechnical calibration data are available. Consistently with these studies, the convergence of independent electrical and seismic anomalies at Fourcare dam provides a more robust indication of anomalous hydro-mechanical conditions than either parameter considered separately. The geological and construction setting at Fourcare dam nevertheless differs substantially from many previously investigated dams. The embankment consists of heterogeneous, reworked sandy-silty glacial deposits overlying undisturbed glacial sediments and fractured serpentinite bedrock. Furthermore, the presence of an internal geomembrane distinguishes the site from structures in which reservoir water directly infiltrates the embankment body. Groundwater recharge from the surrounding alpine catchment may therefore contribute to the conductive domains independently of leakage from the reservoir. These geological, hydrogeological, and construction-specific factors limit the direct transfer of interpretations from other case studies and emphasize the need for site-specific multiparametric evaluations.

The electrical response observed at Fourcare dam is also broadly consistent with previous ERT investigations of seepage and internal erosion in embankment dams and levees. Conductive anomalies have frequently been associated with increased saturation, preferential flow, and sectors potentially affected by internal erosion (Martínez-Moreno et al., 2018; Shin et al., 2019; Masi et al., 2020; Norooz et al., 2024).

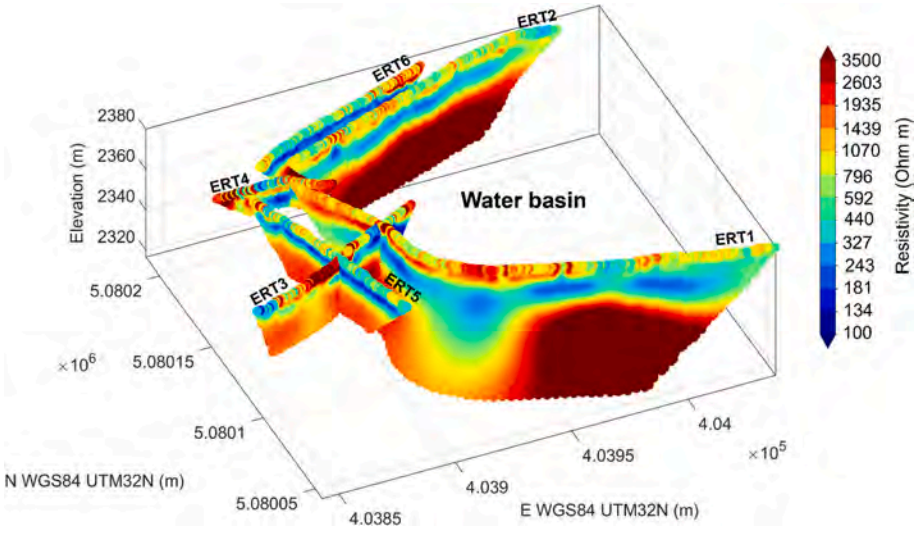


Fig. 8. Three-dimensional visualization of the ERT results for all survey lines obtained using a mixed Wenner–Schlumberger and dipole–dipole configuration.

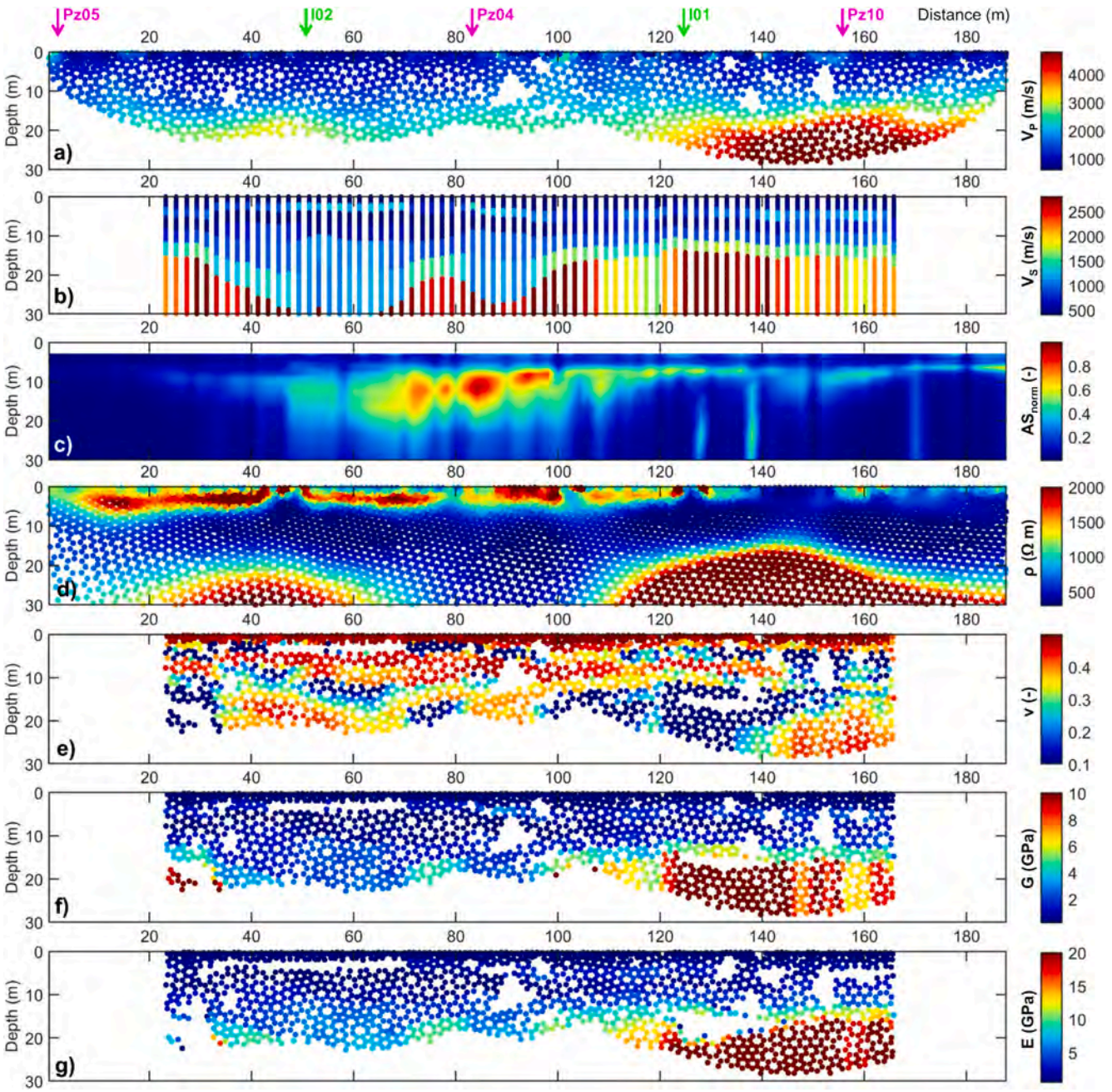


Fig. 9. Results along the seismic line S1-S2: (a) P-wave velocity model; (b) S-wave velocity model; (c) autospectrum. (d) Resistivity results of line ERT1. (e) Poisson ratio, (f) shear modulus, (g) Young's modulus for the grid nodes with available P- and S- velocity estimates, computed considering a constant density of 1900 kg/m^3.

In controlled physical models and time-lapse investigations, resistivity variations have been used to track the development of wetting fronts, suffusion, and piping-related processes (Shin et al., 2019; Masi et al., 2020). However, these studies also show that the electrical response to internal erosion is not necessarily unique. Increased saturation and porosity may reduce resistivity, whereas the selective removal of electrically conductive fine particles may locally produce an increase in resistivity (Martínez-Moreno et al., 2018). Moreover, three-dimensional ERT monitoring of selected test sites demonstrated that anomalies associated with predefined defects may coexist with resistivity variations caused by temperature, construction heterogeneity, embedded structures, and natural variations in water content (Norooz et al., 2024). Consequently, the conductive zones identified at Fourcare dam should be interpreted as evidence of anomalous moisture distribution rather than as a diagnostic signature of active piping or internal erosion. Their spatial association with surface seepage and inclinometer displacement nevertheless increases their engineering relevance.

In detail, the spatial correspondence between low resistivity, reduced shear-wave velocity, high Poisson's ratio, and elevated autospectral values suggests the presence of mechanically weaker and potentially water-saturated materials within the dam body. The elevated Poisson's ratio values (0.4–0.5) support the interpretation of increased pore fluid content. Elevated autospectral amplitudes are associated with zones of lower velocity and reduced mechanical stiffness, where surface waves tend to exhibit higher amplitudes. This behaviour provides a physically consistent basis for interpreting autospectral anomalies as indicators of mechanically weaker or potentially saturated materials within the embankment (Colombero et al., 2019).

The observed multiparametric signature is compatible with hydro-mechanical degradation mechanisms described in previous studies,

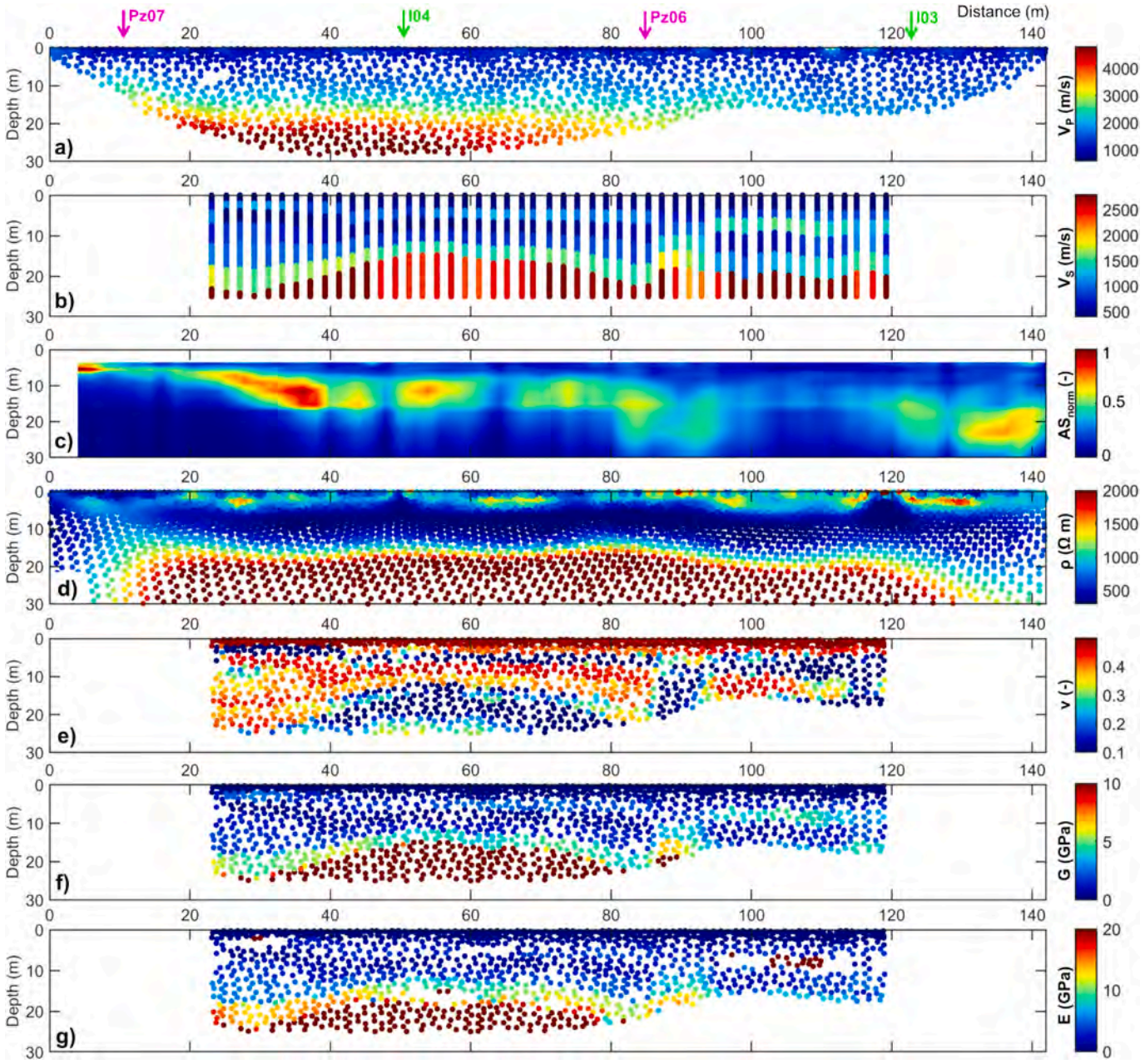


Fig. 10. Results along the seismic line S3: (a) P-wave velocity model; (b) S-wave velocity model; (c) autospectrum. (d) Resistivity results of line ERT2. (e) Poisson ratio, (f) shear modulus, (g) Young's modulus for the grid nodes with available P- and S- velocity estimates, computed considering a constant density of 1900 kg/m^3.

although it cannot be attributed uniquely to a specific process. Increased saturation can reduce electrical resistivity and contribute to lower effective stress and mechanical stiffness, while loosening, cracking, loss of fines, differential settlement, or incomplete compaction may also reduce seismic velocities. The combined occurrence of low resistivity and low V_S therefore indicates a water-affected and mechanically less competent domain, but does not by itself distinguish among seepage-induced softening, internal erosion, construction heterogeneity, and deformation-related changes in permeability. This distinction is particularly important because seepage and deformation may interact through a two-way feedback: preferential flow can promote softening and deformation, while deformation can generate or enlarge preferential hydraulic pathways.

The observed geophysical response is also consistent with the expected transition between the compacted embankment fill and the underlying undisturbed glacial deposits. In addition to interface effects, internal heterogeneities in grain size distribution and degree of compaction within the embankment fill may also contribute to the development of locally weaker zones. The mechanical contrast at this interface may promote stress concentration and localized deformation, while the heterogeneous permeability of glacial deposits may facilitate the development of preferential flow pathways for water infiltration and localized seepage. Decreases in water table depth may also locally increase effective stresses and potentially contribute to deformation; however, this mechanism is not directly constrained by the available data. The deformation patterns observed in the inclinometer data further support the interpretation based on geophysical anomalies. Along line S1–S2, the depth interval affected by displacements observed by I02 coincides with the zone of low shear-wave velocity and high autospectral values, suggesting a link between geophysical anomalies and localized deformation. In contrast, inclinometer I01, located in an area where these anomalies are less pronounced, does not show

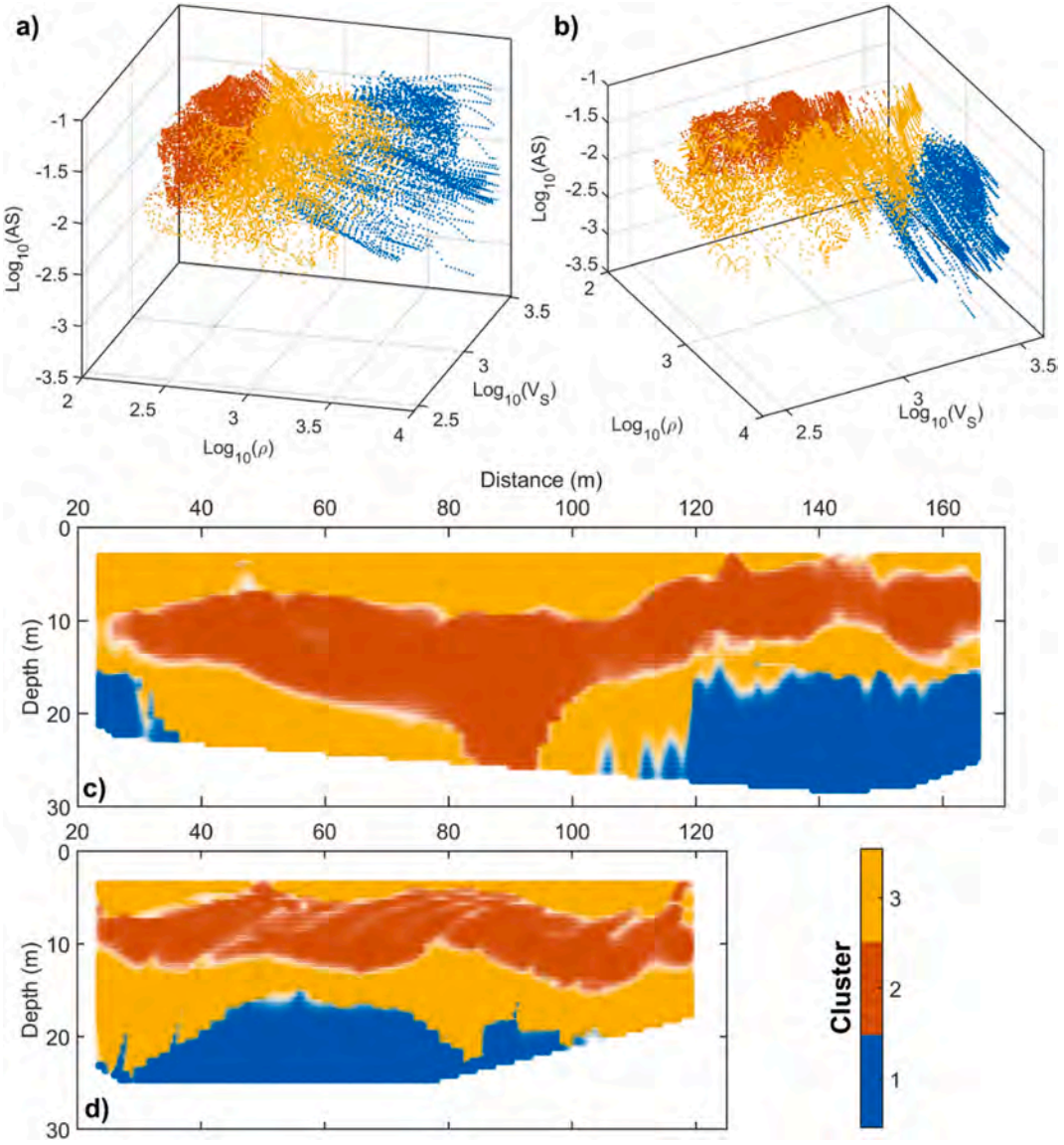


Fig. 11. Clustering of electrical resistivity, shear-wave velocity and autospectral values obtained along lines S1-S2 (ERT1) and S3 (ERT2). The distribution of the clusters is shown in (a) and (b) in 3D. Cluster location along sections S1-S2 (c) and S3 (d). The transparency of each pixel is scaled according to the probability of belonging to a specific cluster (pixels with $P \leq 0.5$ are fully transparent, while those with $P = 1$ appeared fully opaque).

Table 2
Median values of electrical resistivity, shear-wave velocity and autospectral density for each GMM cluster, and proportion of observations assigned to each cluster.

Cluster	Resistivity (Ω • m)	V_S (m/s)	Autospectral density (−)	Observations (%)
1	2707	2474	0.007	20.0
2	351	892	0.029	38.5
3	772	1096	0.018	41.5

significant localized deformation, indicating more stable conditions in that sector.

Previous attempts to integrate multiple geophysical parameters have used joint inversion, structurally coupled inversion, petrophysical relationships, or post-inversion clustering. Penta de Peppo et al. (2024), for example, combined cross-gradient joint inversion of ERT and seismic refraction data with fuzzy clustering to improve structural reconstruction and quantify membership to different geophysical domains. De Donno et al. (2024) applied fuzzy clustering to integrated multiparameter tomographic datasets, using membership functions to detect and localize geophysical targets. These studies demonstrate that clustering can reduce the subjectivity inherent in the visual comparison of separate geophysical models, particularly when supported by borehole information or independently defined targets.

The workflow adopted here differs from these approaches because the electrical and seismic datasets were inverted independently and subsequently integrated using a Gaussian Mixture Model. The GMM does not impose structural similarity between the models during inversion and does not require a deterministic petrophysical relationship among resistivity, V_S, and autospectral density. Instead, it identifies recurrent combinations of geophysical properties while accounting for their covariance and assigns a posterior membership probability to each observation. The inclusion of autospectral density is an additional novel and distinctive element, as it integrates a rapidly computed surface-wave attribute sensitive to lateral variations in weak and low-velocity materials with conventional resistivity and shear-wave velocity models. The methodological advancement therefore lies in the probability-based post-inversion integration of moisture-sensitive and stiffness-sensitive geophysical parameters and attributes for a small

high-altitude embankment characterized by sparse direct information.

While the analysis of individual geophysical parameters already identifies a zone of anomalous conditions, interpreting their spatial distribution across multiple sections and parameter combinations through visual inspection alone remains challenging. The GMM clustering addresses this limitation by providing a spatially coherent, multivariate synthesis of the dataset. This approach enables a more objective discrimination of subsurface domains than would be possible by comparing individual parameter sections separately and allows a direct spatial comparison between the two investigated sections. In this sense, each cluster represents a distinct combination of geophysical properties, reflecting variations in mechanical and moisture conditions, rather than discrete material units. Given the intrinsic heterogeneity of embankment materials and the lack of direct ground truth, these clusters should be interpreted as indicative of consistent patterns within the multiparametric geophysical dataset, rather than as a strictly validated material classification. The quantitative cluster-quality indicators support this interpretation. The generally high posterior probabilities indicate that most observations are consistently assigned within the fitted probabilistic model. Conversely, the moderate global silhouette coefficient and the presence of negative silhouette values for approximately 10% of the observations reveal partial overlap among the identified domains. Such overlap is physically plausible because moisture content, compaction, grain-size distribution, and mechanical stiffness are expected to vary continuously within the heterogeneous embankment fill and glacial deposits. The clustering can therefore be considered an internally consistent probabilistic partition of the multiparametric geophysical space, but not a demonstration that the three clusters correspond to sharply bounded or independently validated material units.

Cluster 1, characterized by higher resistivity and V_S values and lower autospectral amplitudes, reflects mechanically stiffer and less saturated conditions, consistent with more competent conditions at depth. Cluster 3 presents intermediate geophysical properties and appears both in the shallow portion of the embankment and below cluster 2 in both investigated sections, suggesting it reflects heterogeneous conditions rather than a single material unit. Cluster 2, distinguished by lower resistivity and higher autospectral amplitudes, represents the most anomalous domain, consistent with increased moisture content and reduced mechanical properties.

The spatial distribution of cluster 2 differs significantly between the two investigated sections, providing the clearest distinction between their respective internal conditions. Along section S3, its lateral continuity suggests a confined structure within the dam body, which does not support the presence of a direct hydraulic connection between the artificial reservoir and the adjacent natural lake. Inclinometer I03, located along this section, records displacements within the 6–12 m depth interval consistent with deformation at the fill-foundation interface. However, the absence of surface seepage and the coherent clustering pattern suggest that these displacements more likely reflect differential settlement rather than active seepage processes. Along section S1–S2, cluster 2 shows greater lateral variability in thickness and continuity, suggesting a more heterogeneous internal structure. Surface seepage observed on the embankment face is spatially coincident with the sectors where cluster 2 reaches greater depths and shows higher lateral variability, supporting the interpretation of preferential flow pathways in this area. Additionally, the localized deformation recorded by inclinometer I02 within the 5–8 m depth interval occurs immediately above the uppermost boundary of cluster 2, suggesting that deformation concentrates at the contact between the overlying embankment materials and the underlying anomalous zone. These interpretations are supported by the restriction of the clustering analysis to the central portion of the investigated sections, where electrical resistivity, shear-wave velocity, and autospectral density data overlap and exhibit the highest data coverage and reliability, thereby minimizing the influence of potential edge-related effects and limiting their impact on the clustering results.

The interpretation of seepage processes and deformation patterns remains inherently uncertain, given the heterogeneous nature of the glacial deposits and embankment fill and the indirect nature of geophysical measurements. This limitation is consistent with previous studies showing that similar electrical and seismic responses may be produced by different combinations of saturation, temperature, grain-size distribution, porosity, compaction, and damage. Furthermore, unlike time-lapse ERT investigations specifically designed to follow the evolution of wetting fronts or internal erosion, the present single-time survey cannot establish whether the identified anomalies are stable, seasonally variable, or progressively evolving. While multi-parameter consistency improves confidence in the interpretation, the causal relationship between seepage and deformation cannot be established from the available data alone. Seepage may promote deformation, but deformation may equally affect the integrity of the geomembrane and trigger localized leakage. As the geophysical survey lines do not intersect the geomembrane lining, the location of potential breaches cannot be directly constrained by the available data. Infiltration may not necessarily result from a discrete failure of the geomembrane but could originate at structurally more delicate locations such as seams, or structural penetrations, where localized leakage may occur even in the absence of a well-defined breach. In such a scenario, preferential flow through the heterogeneous glacial deposits may then govern water redistribution, potentially explaining the spatial concentration of geophysical anomalies and surface seepage observed in the western sector.

The integrated approach applied in this study, serves as a primary screening tool, identifying spatially coherent zones that may require targeted monitoring and further investigations, rather than quantifying the severity of the process involved. While the multi-parameter analysis provides a consistent framework for interpreting hydro-mechanical conditions within the embankment, a more detailed assessment would require complementary data, including time-lapse geophysical monitoring, geotechnical and hydraulic measurements, geomembrane integrity testing, and analyses of hydraulic connectivity.

From an engineering geology perspective, the broader relevance of the proposed workflow lies in its ability to transform complementary geophysical measurements into spatially explicit and uncertainty-aware hydro-mechanical domains. This is particularly valuable for small and remote alpine embankments, where direct geotechnical information and permanent monitoring systems are commonly sparse. The resulting classification can support the prioritization of detailed inspections and complementary investigations by identifying sectors in which independent electrical, seismic, and deformation-related evidence converge. Future time-lapse surveys acquired under comparable thermal and hydrological conditions would allow the spatial baseline established here to be developed into a monitoring framework capable of distinguishing reversible seasonal variability from progressive hydro-mechanical degradation.

6. Conclusions

This study demonstrates the potential of an integrated geophysical approach combining electrical resistivity tomography and active seismic methods for the characterization of a small alpine earthen dam.

The results reveal the presence of a shallow unsaturated layer overlying zones of lower resistivity, reduced shear-wave velocity, and higher autospectral values, interpreted as areas of increased moisture content and reduced stiffness. These features are particularly evident in the western sector (section S1-S2), suggesting potentially more critical conditions. In contrast, in the northern sector (section S3), the clustering results do not support the presence of a direct hydraulic connection between the investigated reservoir and the adjacent natural lake.

The integration of geophysical parameters through a GMM clustering framework enabled the identification of spatially coherent domains

within the embankment, providing a unified representation of subsurface conditions and improving the detection of hydraulic and mechanical heterogeneities compared to individual methods.

Although the interpretation is affected by uncertainties related to material heterogeneity and the lack of direct ground truth, the integrated approach identifies potentially critical zones and provides a valuable basis for targeted monitoring. Overall, the proposed methodology represents a valuable tool for the non-invasive assessment of remote embankment dams, particularly in high-mountain environments where traditional monitoring approaches may be limited.

CRediT authorship contribution statement

Valeria Strallo: Writing – review & editing, Writing – original draft, Investigation, Data curation, Conceptualization. **Chiara Colombero:** Writing – review & editing, Supervision, Investigation, Data curation, Conceptualization. **Alberto Godio:** Writing – review & editing, Supervision, Project administration, Funding acquisition, Conceptualization.

Declaration of competing interest

The authors declare that they have no known competing financial interests or personal relationships that could have appeared to influence the work reported in this paper.

Acknowledgments

The authors are in debt with Diego Franco, Andrea Vergnano and Stefano Vigna for their valuable support in data acquisition. The authors also thank Società Monterosa S.p.A. for providing documentation and key information supporting the characterization of the alpine study site, and, in particular, Pierluigi Orru for his insightful discussions. They further thank Ufficio Dighe della Regione Valle d'Aosta for their support.

This publication is part of the project PNRR-NGEU which has received funding from the MUR-DM 118/2023. The research activities of this paper were funded by the NODES project, which has received funding from the MUR-M4C2 1.5 of PNRR funded by the European Union - NextGenerationEU (grant agreement no. ECS00000036).

Data availability

The meteorological data are accessible at https://presidi2.regione.vda.it/str_dataview_download. All other data are available upon request by contacting the corresponding author.

References

Adamo, N., Al-Ansari, N., Sissakian, V., Laue, J., Knutsson, S., 2020. Geophysical methods and their applications in dam safety monitoring. J. Earth Sci. Geotech. Eng. 11, 291–345. https://doi.org/10.47260/jesge/1118.

Al-Janabi, A.M.S., Ghazali, A.H., Ghazaw, Y.M., Afan, H.A., Al-Ansari, N., Yaseen, Z.M., 2020. Experimental and numerical analysis for earth-fill dam seepage. Sustainability 12 (6), 2490. https://doi.org/10.3390/su12062490.

Auken, E., Christiansen, A.V., 2004. Layered and laterally constrained 2D inversion of resistivity data. Geophysics 69. https://doi.org/10.1190/1.1759461.

Ayadat, T., 2019. Causes of embankment failure. J. Sci. Eng. Res. 6 (2), 249–251.

Baxter, R.M., 1977. Environmental effects of dams and impoundments. Annu. Rev. Ecol. Syst. 8, 255–283.

Blanchy, Guillaume, Saneiyan, Sina, Boyd, Jimmy, McLachlan, Paul, Binley, Andrew, 2020. ResIPy, an intuitive open source software for complex geoelectrical inversion/modeling. Computers & Geosciences 137, 104423. https://doi.org/10.1016/j.cageo.2020.104423. https://linkinghub.elsevier.com/retrieve/pii/S0098300419308192, 104423.

Bocchiola, D., Rosso, R., 2014. Safety of Italian dams in the face of flood hazard. Adv. Water Resour. 71, 23–31. https://doi.org/10.1016/j.advwatres.2014.05.006.

Boiero, D., 2009. Surface Wave Analysis for Building Shear Wave Velocity Models. PhD thesis. Politecnico di Torino, 233 pp.

Bozzoni, F., Misiano, G., Lai, C.G., 2023. A multi-scale tool for assessing the seismic risk of small dams during emergency preparedness and response phase. Nat. Hazards 118 (3), 2069–2095. https://doi.org/10.1007/s11069-023-06081-z.

Camarero, P.L., Moreira, C.A., 2017. Geophysical investigation of earth dam using the electrical tomography resistivity technique. REM - Int. Eng. J. 70 (1), 47–52. https://doi.org/10.1590/0370-44672016700099.

Cardarelli, E., Cercato, M., De Donno, G., 2014. Characterization of an earth-filled dam through the combined use of electrical resistivity tomography, P- and SH-wave seismic tomography and surface wave data. J. Appl. Geophys. 106, 87–95. https://doi.org/10.1016/j.jappgeo.2014.04.007.

Ciancimino, A., Cosentini, R.M., Figura, F., Foti, S., 2023. Simplified assessment of the seismic vulnerability of small earth dams. Procedia Struct. Integrity 44, 323–330. https://doi.org/10.1016/j.prostr.2023.01.042.

Colombero, C., Comina, C., Socco, L.V., 2019. Imaging near-surface sharp lateral variations with surface-wave methods – part 1: detection and location. Geophysics 84 (6), EN93–EN111. https://doi.org/10.1190/geo2019-0149.1.

De Donno, G., Cercato, M., Melegari, D., Paoletti, V., Penta de Peppo, G., Piegari, E., 2024. Fuzzy mapping of integrated multiparameter tomographic data to detect and localize geophysical targets. IEEE Trans. Geosci. Remote Sens. 62. https://doi.org/10.1109/TGRS.2024.3445462.

Duvillard, P.-A., Ravanel, L., Marcer, M., Schoeneich, P., 2019. Recent evolution of damage to infrastructure on permafrost in the French Alps. Reg. Environ. Chang. 19 (5), 1281–1293. https://doi.org/10.1007/s10113-019-01465-z.

Food and Agriculture Organization of the United Nations (FAO), 2010. Manual on small earth dams: A guide to siting, design and construction. In: FAO Irrigation and Drainage Paper 64.

Gruber, S., Hoelzle, M., Haeberli, W., 2004. Permafrost thaw and destabilization of alpine rock walls in the hot summer of 2003. Geophys. Res. Lett. 31 (13), L13504. https://doi.org/10.1029/2004GL020051.

Himi, M., Casado, I., Sendrós, A., Lovera, R., Rivero, L., Casas, A., 2018. Assessing preferential seepage and monitoring mortar injection through an earthen dam settled over a gypsiferous substrate using combined geophysical methods. Eng. Geol. 246, 212–221. https://doi.org/10.1016/j.enggeo.2018.10.002.

IPCC, 2019. Summary for policymakers. In: Pörtner, H.-O., Roberts, D.C., Masson-Delmotte, V., Zhai, P., Tignor, M., Poloczanska, E., Mintenbeck, K., Alegría, A., Nicolai, M., Okem, A., Petzold, J., Rama, B., Weyer, N.M. (Eds.), IPCC Special Report on the Ocean and Cryosphere in a Changing Climate.

Kasana, A., Minárik, M., Nikolaj, M., 2015. Impact of geotechnical factors on the safety of low embankment dams from the perspective of technical and safety supervision. Slovak J. Civ. Eng. 23. https://doi.org/10.1515/sjce-2015-0002.

Kayode, O.T., Odukoya, A.M., Adagunodo, T.A., Adeniji, A.A., 2018. Monitoring of seepages around dams using geophysical methods: a brief review. IOP Conf. Ser.: Earth Environ. Sci 173 (1), 012026. https://doi.org/10.1088/1755-1315/173/1/012026.

Khosro Anjom, F., Adler, F., Socco, L.V., 2024. Comparison of surface-wave techniques to estimate S- and P-wave velocity models from active seismic data. Solid Earth 15 (3), 367–386. https://doi.org/10.5194/se-15-367-2024.

Koyama, A., Fujimoto, T., Suetsugu, D., Fukubayashi, Y., 2022. Analysis of embankment failure mechanism in reservoirs due to rainfall infiltration during heavy rainfall. Geomat. Nat. Haz. Risk 13 (1), 1849–1866. https://doi.org/10.1080/19475705.2022.2102440.

Li, Z., Ye, W., Marence, M., Bricker, J.D., 2019. Unsteady seepage behavior of an earthfill dam during drought-flood cycles. Geosciences 9 (1), 1. https://doi.org/10.3390/geosciences9010017.

Linde, N., Doetsch, J., 2016. Joint inversion in hydrogeophysics and near-surface geophysics. In: Integrated Imaging of the Earth. American Geophysical Union (AGU), pp. 117–135. https://doi.org/10.1002/9781118929063.ch7.

Liu, J., Yu, J., Hu, S., Hu, C., Wang, J., Yu, Z., Huang, K., 2024. Analysis of crack evolution of expansive soil embankment under extreme arid climate. Case Stud. Constr. Mater. 20, e02902. https://doi.org/10.1016/j.cscm.2024.e02902.

Loperte, A., Soldovieri, F., Palombo, A., Santini, F., Lapenna, V., 2016. An integrated geophysical approach for water infiltration detection and characterization at Monte Cotugno rock-fill dam (southern Italy). Eng. Geol. 211, 162–170. https://doi.org/10.1016/j.enggeo.2016.07.005.

Martínez-Moreno, F.J., Delgado-Ramos, F., Galindo-Zaldívar, J., Martín-Rosales, W., López-Chicano, M., González-Castillo, L., 2018. Identification of leakage and potential areas for internal erosion combining ERT and IP techniques at the Negratín Dam left abutment (Granada, southern Spain). Eng. Geol. 240, 74–80. https://doi.org/10.1016/j.enggeo.2018.04.012.

Masi, M., Ferdos, F., Losito, G., Solari, L., 2020. Monitoring of internal erosion processes by time-lapse electrical resistivity tomography. J. Hydrol. 589, 125340. https://doi.org/10.1016/j.jhydrol.2020.125340.

McLachlan, G., Peel, D., 2000. Finite Mixture Models. John Wiley & Sons, Inc.

Michalis, P., Sentenac, P., MacBrayne, D., 2016. Geophysical assessment of dam infrastructure: The Mugdock reservoir dam case study. In: Proceedings of the 3rd Joint International Symposium on Deformation Monitoring (JISDM), Vienna, Austria.

Neducza, B., 2007. Stacking of surface waves. Geophysics 72, 51–58. https://doi.org/10.1190/1.2431635.

Norooz, R., Nivorlis, A., Olsson, P.-I., Günther, T., Bernstone, C., Dahlin, T., 2024. Monitoring of Älvkarleby test embankment dam using 3D electrical resistivity tomography for detection of internal defects. J. Civ. Struct. Heal. Monit. 14, 1275–1294. https://doi.org/10.1007/s13349-024-00785-x.

Ólafsdóttir, E.Á., Bessason, B., Erlingsson, S., 2019. Stiffness profiles of earth dams based on the MASW technique. In: Proceedings of the XVII European Conference on Soil Mechanics and Geotechnical Engineering, pp. 3782–3791. https://doi.org/10.32075/17ECSMGE-2019-0788.

Omofunmi, O., Kolo, J., Oladipo, A., Diabana, P., Ojo, A., 2017. A review on effects and control of seepage through earth-fill dam. Curr. J. Appl. Sci. Technol. 22 (5), 1–11. https://doi.org/10.9734/CJAST/2017/28538.

Panthulu, T.V., Krishnaiah, C., Shirke, J.M., 2001. Detection of seepage paths in earth dams using self-potential and electrical resistivity methods. Eng. Geol. 59 (3), 281–295. https://doi.org/10.1016/S0013-7952(00)00082-X.

Park, C.B., Miller, R.D., Xia, J., 1998. Imaging dispersion curves of surface waves on multi-channel record. In: SEG Technical Program Expanded Abstracts 1998, pp. 1377–1380. https://doi.org/10.1190/1.1820161.

Penta de Peppo, G., Cercato, M., De Donno, G., 2024. Cross-gradient joint inversion and clustering of ERT and SRT data on structured meshes incorporating topography. Geophys. J. Int. 239, 1155–1169. https://doi.org/10.1093/gji/ggae326.

Perri, M.T., Boaga, J., Bersan, S., Cassiani, G., Cola, S., Deiana, R., Simonini, P., Patti, S., 2014. River embankment characterization: the joint use of geophysical and geotechnical techniques. J. Appl. Geophys. 110, 5–22. https://doi.org/10.1016/j.jappgeo.2014.08.012.

Pinto, W., Fais, L., 2023. The Small Dams Safety Index (SDSI): a tool for small dams safety assessment. Int. J. River Basin Manag. 21 (3), 551–558. https://doi.org/10.1080/15715124.2022.2047711.

Pisaniello, J.D., Dam, T.T., Tingey-Holyoak, J.L., 2015. International small dam safety assurance policy benchmarks to avoid dam failure flood disasters in developing countries. J. Hydrol. 531, 1141–1153. https://doi.org/10.1016/j.jhydrol.2015.09.077.

Rücker, C., Günther, T., Wagner, F.M., 2017. pyGIMLi: an open-source library for modelling and inversion in geophysics. Comput. Geosci. 109, 106–123. https://doi.org/10.1016/j.cageo.2017.07.011.

Shin, S., Park, S., Kim, J.H., 2019. Time-lapse electrical resistivity tomography characterization for piping detection in earthen dam model of a sandbox. J. Appl. Geophys. 170, 103834. https://doi.org/10.1016/j.jappgeo.2019.103834.

Strozzi, T., Antonova, S., Günther, F., Mätzler, E., Vieira, G., Wegmüller, U., Westermann, S., Bartsch, A., 2018. Sentinel-1 SAR interferometry for surface deformation monitoring in low-land permafrost areas. Remote Sens. 10 (9), 1360. https://doi.org/10.3390/rs10091360.

Vagnon, F., Comina, C., Arato, A., 2022. Evaluation of different methods for deriving geotechnical parameters from electric and seismic streamer data. Eng. Geol. 303, 106670. https://doi.org/10.1016/j.enggeo.2022.106670.

Wu, G., Xie, Y., Wei, J., Yue, X., 2023. Freeze-thaw erosion mechanism and preventive actions of highway subgrade soil in an alpine meadow on the Qinghai–Tibet Plateau. Eng. Fail. Anal. 143, 106933. https://doi.org/10.1016/j.engfailanal.2022.106933.

Yener Ozkan, M., 1998. A review of considerations on seismic safety of embankments and earth and rock-fill dams. Soil Dyn. Earthq. Eng. 17 (7), 439–458. https://doi.org/10.1016/S0267-7261(98)00035-9.

Ziccarelli, M., Rosone, M., 2021. Stability of embankments resting on foundation soils with a weak layer. Geosciences 11 (2), 86. https://doi.org/10.3390/geosciences11020086.